Journal of Materials Chemistry A

ROYAL SOCIETY OF CHEMISTRY

PAPER

View Article Online
View Journal | View Issue

Cite this: J. Mater. Chem. A, 2025, 13, 15659

Computational design of polaronic conductive Li-NASICON mixed ionic–electronic conductors†

Jiawei Lin, [ab] KyuJung Jun *[ab] and Gerbrand Ceder *[ab]

Li-NASICONs featuring three-dimensional corner-sharing frameworks have been experimentally and theoretically demonstrated to be fast Li-ion conductors, with high room-temperature ionic conductivities. In this study, we conduct first-principles calculations to investigate the polaronic conduction in Li-NASICONs comprising different transition metal (TM) elements (Ti, V, Cr, Mn, Fe, Mo) and evaluate their potential as mixed electron-ion conductors. We find that the electron polaron conductivity of octahedral–octahedral (oct–oct) hopping in Li-NASICONs is strongly correlated with the Jahn–Teller activity on the TM site. While $LiMn_2(PO_4)_3$ and $Li_3Cr_2(PO_4)_3$ have a low predicted electron polaron conductivity owing to the J–T distortion resulting from the polaron formation, $LiFe_2(PO_4)_3$ is predicted to have the most facile polaron transport, which stems from the elimination of its intrinsic J–T distortion upon polaron formation. We also find that polaron hopping between octahedral and tetrahedral sites contributes limited electronic conductivity because of the large difference in the polaron formation energies on these sites. For polaron transport along purely tetrahedral sites, we find limited transport through the V^{5+}/V^{4+} pair in $LiGe_2(VO_4)_3$ and $LiTi_2(VO_4)_3$ but better conductivity through the Mo^{6+}/Mo^{5+} pair in $LiTi_2(MoO_4)_3$. Our research suggests that Li-NASICONs with TM elements involving no J–T distortion upon polaron formation on octahedral sites and Mo on tetrahedral sites are promising candidates for mixed ionic electronic conductors (MIECs).

Received 14th January 2025
Accepted 8th April 2025

DOI: 10.1039/d5ta00367a

rsc.li/materials-a

1. Introduction

Many electrochemical energy storage devices require the addition of carbon as a conductive additive to the cathode composite. While carbonaceous materials are inexpensive, they can be the source of degradation phenomena in several new technologies. For example, in solid-state batteries, carbon has been identified as the source of electrochemical breakdown of sulfide solid-state conductors.[1,2] In Li–O_2 batteries, porous carbon cathodes and organic carbonate electrolytes in non-aqueous Li–O_2 batteries are prone to degradation during cycling.[3] The carbonaceous components react with the Li_2O_2 discharge product and form insulating Li_2CO_3 (ref. 4) and reduce the capacity of the cell.[5] In addition, the incorporation of lithium as lithium carbonate at the Li_2O_2–electrolyte interface leads to an increased overpotential during cycling.[6]

To address these issues, attempts have been made to replace carbon in cathodes with other electron-conducting materials,[7] such as noble metals and alloys,[8–11] titanium compounds (oxides,[12,13] carbides,[14] and nitrides[15]), and perovskites in nonaqueous Li–O_2 batteries.[16,17] In addition, solid-state Li–O_2 batteries with Li-NASICON,[18,19] perovskite,[20] and zeolite[21] inorganic electrolytes have also been proposed to avoid Li_2CO_3 formation.

One feasible approach to develop MIECs is to introduce electronic conductivity in crystals that already exhibit high Li-ion conductivity, such as perovskite, garnet, and Li-NASICON. For instance, Ma *et al.* investigated the perovskites Li_xLa_y-MO_{3-z} with various TM elements (M = Ti, Cr, Mn, Fe, and Co) and demonstrated that $Li_{0.34}La_{0.55}MnO_{3-z}$ exhibits high electronic conductivity (2.04×10^{-3} S cm^{-1}) and Li-ion conductivity (8.53×10^{-5} S cm^{-1}).[22] This remarkable electronic conductivity was attributed to the favorable formation of oxygen vacancies, which result in a higher mobile electron concentration in the compound. Kim *et al.*[23] developed a MIEC cathode consisting of electron-conducting RuO_2 and Li-ion conducting La_2LiRuO_{6-x} to enhance the cyclability of solid-state Li–O_2 batteries. Jin *et al.*[24] introduced diverse TM elements (Mn, Fe, Co, Ni) into the Li and Zr sites of garnets and discovered that garnet with Fe in Li sites exhibits high mixed ionic–electronic conductivity ranging from 10^{-5} to 10^{-4} S cm^{-1}. The electronic conduction was attributed to polaronic conduction through the Fe^{2+}–O–Fe^{3+} pathway. Recently, Li-NASICONs with compositions of $LiTi_2(PO_4)_{3-x}(VO_4)_x$ and $Li_{1.3}Al_{0.3}Ti_{1.7}(PO_4)_{3-x}(VO_4)_x$, where x = 0.1, 0.2, 0.3, and 0.4, were shown to display mixed ionic–electronic conductivity ranging between 10^{-5} and 10^{-4} S cm^{-1}, with the

[a]Department of Materials Science and Engineering, University of California, Berkeley, USA. E-mail: gceder@berkeley.edu; kjun@berkeley.edu

[b]Materials Science Division, Lawrence Berkeley National Laboratory, USA

† Electronic supplementary information (ESI) available. See DOI: https://doi.org/10.1039/d5ta00367a

enhanced electronic conductivity being linked to polaronic conduction through the V^{5+}/V^{4+} pair.[25] Previous theoretical work has also reported low polaron hopping barriers in doped $SrCeO_3$ perovskite[26] and Li-Garnet compounds,[27] highlighting the possibility for electronic conduction in wide-band-gap transition metal oxides. Since Li-NASICONs can be synthesized with a diversity of TM on the octahedral and tetrahedral sites,[28–30] we evaluate in this paper the effect of each chemistry on the electronic conductivity.

Polarons are quasiparticles that involve the coupling of excess carriers with lattice vibrations in polarizable materials.[31] Within polarons, holes or electrons are trapped in a local structural distortion. Numerous materials, including inorganic crystals (commonly oxides) and polymers, have been reported to contain polarons induced from a variety of sources, such as oxygen vacancies, photoexcitation, and extrinsic doping.[31] Polarons contribute to electronic conductivity *via* a hopping mechanism, where a localized charge transfers from one atom to another assisted by the transport of the lattice distortion and the tunneling of the charge between two atomic sites.

In this study, we investigate polaronic conduction in Li-NASICONs with different transition metal (TM) elements (Ti, V, Cr, Mn, Fe, Mo) using first-principles calculation. We first compute the polaron formation energies in Li-NASICONs and find that all Li-NASICONs except $Li_3Fe_2(PO_4)_3$ have negative electron polaron-formation energies, indicating the favorable existence of electron polarons in the compounds. Next, we identify percolating conduction paths in Li-NASICONs and calculate their rate-determining hopping barriers for oct–oct, oct–tet, and tet–tet polaronic conduction. We use the computed hopping barriers and the electronic coupling between the initial and final polaronic state to estimate the room-temperature polaronic conductivity of Li-NASICONs. Our study suggests that Li-NASICONs with TM elements involving no J–T distortion upon polaron formation on octahedral sites or with Mo on tetrahedral sites to be promising candidates for MIECs.

2. Computational methodology

To localize an electron polaron in electronic structure methods, self-interaction needs to be fully or partially removed. Density functional theory (DFT) with a Hubbard-*U* correction or hybrid functionals are commonly adopted to reduce the charge self-interaction[32–37] for systems with d- or f-band electrons. The DFT+*U* scheme requires an appropriate selection of the Hubbard-*U* value for a reliable description of the d- or f-band electronic structure, which typically involves fitting theoretically predicted physical properties against their experimental counterparts. This process renders a different set of +*U* potentials for different physical properties and compounds, and the calculated polaron formation energy or hopping barrier is susceptible to change with +*U* potentials.[38,39] In contrast, hybrid functionals involve fewer empirical parameters to obtain localized polaronic solutions[40] and have been reported to be more successful in obtaining localized solutions than the DFT+U scheme.[41] Hence, in this study, we adopt the HSE06 hybrid functional[42] for all calculations, including the optimization of the polaron structure, its hopping barrier, and the projected crystal orbital Hamilton population (p-COHP) of the polaronic orbitals on the neighboring TM atoms. All the calculations are performed using the Vienna *ab initio* simulation package (VASP),[43–45] and the input generation is performed using the Pymatgen library.[46]

To model the formation of a polaron, lattice-parameter optimizations for all neutral Li-NASICONs are first conducted. Subsequently, we add an extra electron to a Li-NASICON supercell containing 72 oxygens and perform geometrical optimization of the supercell with an excess electron with the lattice parameters of the cell fixed to those of the neutral cell. To more easily converge to a polaronic state, we introduce a structural perturbation to a TM–O_6 octahedron and a TM–O_4 tetrahedron by elongating each of the six and four TM–O bonds by 10%. This bond-distortion approach has been extensively used to break the symmetry of a crystal and facilitates electronic density localization on a polaronic site.[47–54] We note that initial bond distortions are only applied on the TM-site with an electron polaron. In addition, to promote the localization of an electron at the specified TM-site, we initialize the magnetic moment of the TM atom containing the polaron to be $1\mu_B$ higher than those of the other TM atoms. To obtain a delocalized electronic structure, we add one excess electron to each Li-NASICON compound without bond distortion and initialization of the magnetic moments for TM atoms, which facilitates the optimization of the non-polaronic structure. For all DFT calculations, an energy cutoff of 520 eV is used for the plane-wave basis set, and a gamma-point-only K-point grid[55] is adopted. The convergence criteria for electronic and ionic steps are set to 10^{-5} eV for energy and 0.01 eV $Å^{-1}$ for force, respectively.

Polaron transport is studied using a linear-interpolation method to describe the transfer of lattice distortion[56–62] between two sites. In this approach, the intermediate images of the hopping trajectory $\{q_x\}$ are obtained by linearly interpolating the initial $\{q_i\}$ and final $\{q_f\}$ optimized polaronic structures, *i.e.*, $\{q_x\} = (1 - x)\{q_i\} + x\{q_f\}$, where $0 < x < 1$. In this study, seven intermediate images are used to locate the transition state and determine the kinetic barrier of each hop. We also initialize the magnetic moments of the two TM atoms that participate in a hop in the seven intermediate images as a linear interpolation between the magnetic moments of the two TM atoms in the initial and final polaronic structures for Fe- and Mn-containing Li-NASICONs. This magnetic moment initialization serves only to guide the convergence of the electronic structure of the intermediate images along the minimum energy pathways and does not constrain the magnetic moments during the optimization of the reaction pathway.

Although the linear interpolation approach may not always be valid for long-range polaron hops, we expect that it remains a reasonable approximation for simulating such hops in Li-NASICONs. To validate this, we perform a CI-NEB calculation for the longest hop (Hop IV) in $LiTi_2(PO_4)_3$, which has a hopping distance of 6.02 Å, using seven images and a force convergence criterion of 0.02 eV $Å^{-1}$. Notably, the hopping barrier obtained from the CI-NEB method is 0.27 eV, closely matching the 0.28 eV barrier obtained using the linear interpolation approach for the

same hop. This suggests that the linearly interpolated images are already close to the minimum energy path for the hop. Therefore, we believe this approach reasonably captures the lattice distortion geometry during long-range hopping in Li-NASICON, although a more accurate hopping barrier can be obtained using the CI-NEB method at the expense of significantly higher computational cost.

We investigate the electron polaron transport for Li-NASICONs in the well-studied structure of $LiTi_2(PO_4)_3$, which has a trigonal lattice with space group $R\bar{3}C$. The chemical space is explored by replacing different elements in octahedral or tetrahedral sites. Although Li-NASICONs can form in other structures (monoclinic,[63] triclinic,[64] and orthorhombic[65]), the topologies of the corner-sharing framework consisting of MO_6 octahedra and PO_4 tetrahedra are similar to those of trigonal Li-NASICONs.[66]

In the three-dimensional corner-sharing framework of Li-NASICONs, the octahedral sites can accommodate various TMs, including Ti, V, Cr, Mn, Fe, and Co. In contrast, the tetrahedral sites are usually occupied by main group cations (*e.g.* P, Si), though some fully oxidized TM such as V and Mo can occasionally also be accommodated on these sites. We study eleven different Li-NASICONs, eight of which contain one Li atom with the other three containing three Li atoms per formula unit in the $R\bar{3}C$ and $R\bar{3}$ space group, respectively. We exclude Co-containing Li-NASICONs in this work as we are not able to localize an electron polaron to form a Co^{3+} in Co^{4+}-containing Li-NASICON, which may be related to the ability of Co^{4+} to become metallic in oxides.[67,68] In this study, we only consider electron polarons as a previous work by Kaur *et al.*[69] found in V-oxides that electron and hole polarons behave similarly.

3. Results

3.1. Polaron formation in Li-NASICONs

The localization of a polaron causes the TM–O bonds of the TM in the polaronic site to elongate and the magnetic moment on the TM to increase by approximately $1\mu_B$. The TM–O bond lengths and the magnetic moments of the TM atoms before and after polaron formation in Li-NASICONs are shown in Fig. S1.† The computed polaron formation energies (E_P) of each Li-NASICON, as well as the space group and the source of each crystal model are listed in Table 1. E_P is calculated as the energy difference between the polaronic and delocalized solution, *i.e.*, $E_P = E_{localized} - E_{delocalized}$. This value is negative for all the Li-NASICONs considered (Table 1), indicating favorable polaron formations in all compounds, consistent with our expectation. For $Li_3Fe_2(PO_4)_3$, we successfully find a localized solution, indicating that the formation of a polaron in this structure is feasible, although the formation energy could not be determined as we are unable to converge a delocalized solution for $Li_3Fe_2(PO_4)_3$. The formation energy of an electron polaron on Ti^{4+} is among the least negative ones, consistent with it being an early transition metal with more extended d-orbitals and its tendency in oxides to often become metallic when partially reduced. The electrochemical stability windows of Li-NASICONs, computed with the previous defined formalism,[71–73] are listed in the Table S3.† These values are calculated without considering the possibility of Li (de)intercalation, which may occur due to the mixed ionic–electronic conductivity. Details of the methodology are provided in the ESI.†

3.2. Percolating paths for polaronic conduction in Li-NASICONs

Polarons must have percolating paths through the entire structure to enable overall conduction. The Li-NASICONs which contain one Li per formula unit, namely $Li(TM/Ge)_2((P/V/Mo)O_4)_3$, contain only one symmetrically distinct octahedral (12c) and tetrahedral site (18e) to accommodate TM atoms. In these cases, we find that an electron polaron can be localized on each TM atom. However, for Li-NASICONs with compositions $Li_3TM_2(PO_4)_3$, there are two symmetrically distinct octahedral TM sites in the $R\bar{3}$ space group. We find that the less distorted octahedral TM site (6c1) (edge-sharing with $Li–O_4$ tetrahedra) is able to accommodate localized charge, whereas the more

Table 1 Polaronic site, polaron formation energy (E_P), space group (S.G.), energy above the hull, and source of the crystal model of Li-NASICONs. "mp" refers to the Materials Project id numbers.[70] Energy above the hull values marked with an asterisk are obtained from our DFT calculations using the GGA/GGA+*U* functional, while those without an asterisk are extracted directly from the Materials Project

	Polaronic site	Valence state	E_P (eV)	S. G.	Crystal model source	Energy above the hull (eV per atom)
$LiTi_2(PO_4)_3$	Octahedral	Ti^{4+}/Ti^{3+}	−0.42	$R\bar{3}C$	mp – 18640	0
$LiV_2(PO_4)_3$	Octahedral	V^{4+}/V^{3+}	−0.52	$R\bar{3}C$	mp – 26712	0.002
$LiCr_2(PO_4)_3$	Octahedral	Cr^{4+}/Cr^{3+}	−0.54	$R\bar{3}C$	mp – 25838	0.044
$LiMn_2(PO_4)_3$	Octahedral	Mn^{4+}/Mn^{3+}	−0.60	$R\bar{3}C$	Replace Ti with Mn in $LiTi_2(PO_4)_3$	0.012*
$LiFe_2(PO_4)_3$	Octahedral	Fe^{4+}/Fe^{3+}	−1.71	$R\bar{3}C$	mp – 26581	0.079
$Li_3Ti_2(PO_4)_3$	Octahedral	Ti^{3+}/Ti^{2+}	−0.16	$R\bar{3}$	mp – 26883	0.064
$Li_3Cr_2(PO_4)_3$	Octahedral	Cr^{3+}/Cr^{2+}	−0.33	$R\bar{3}$	mp – 26971	0
$Li_3Fe_2(PO_4)_3$	Octahedral	Fe^{3+}/Fe^{2+}	—	$R\bar{3}$	mp – 19430	0.010
$LiTi_2(VO_4)_3$	Octahedral	V^{5+}/V^{4+}	−0.21	$R\bar{3}C$	Replace P with V in $LiTi_2(PO_4)_3$	0.005*
$LiTi_2(VO_4)_3$	Tetrahedral	V^{5+}/V^{4+}	−0.61	$R\bar{3}C$	Replace P with V in $LiTi_2(PO_4)_3$	
$LiGe_2(VO_4)_3$	Tetrahedral	V^{5+}/V^{4+}	−0.71	$R\bar{3}C$	Replace Ti with Ge in $LiTi_2(VO_4)_3$	0.008*
$LiTi_2(MoO_4)_3$	Tetrahedral	Mo^{6+}/Mo^{5+}	−0.39	$R\bar{3}C$	Replace P with Mo in $LiTi_2(PO_4)_3$	0.132*

distorted octahedral TM site (6c2) (corner-sharing with Li–O_4 tetrahedra) cannot accommodate a polaron. Consequently, fewer polaron hops are available in $Li_3TM_2(PO_4)_3$ than in $LiTM_2(PO_4)_3$. The octahedral TM sites that can accommodate polaron are visualized in Fig. 1b.

In this work, we first determine the polaron hops between two neighboring TMs with hopping distances of less than 7 Å. This includes hops between octahedral sites, octahedral-to-tetrahedral, as well as between tetrahedral sites. We exclude hops with hopping distances of more than 7 Å, as these hops are combinations of shorter hops. In addition, the tunneling probability of a hop between two TM atoms exponentially decays with respect to the hopping distance. All the hops considered are either perpendicular or parallel to [001] direction, which aligns with the *z*-axis of the Li-NASICON crystal structure, as shown in Fig. 1. While most ions in our compounds have reasonable valence states for the coordination they occupy, $LiTi_2(MoO_4)_3$ with both Mo^{6+} and Mo^{5+} on the tetrahedral site is introduced as a more hypothetical compound, as Mo^{5+} is unlikely to be found on a tetrahedral site.[74,75] The ground-state electronic structure of $LiTi_2(MoO_4)_3$ exhibits magnetic moments of $0.90\mu_B$ on each Ti ion, suggesting a valence +3. To maintain charge neutrality, the average valence of Mo atoms is then +17/3, which contain one-third Mo^{5+} and two-thirds Mo^{6+}, consistent with the magnetic moments of $0.78\mu_B$ and $0.09\mu_B$ found in the calculations. We find that an electron polaron in this compound preferentially localizes on Mo^{6+}, as evidenced by the electron polaron formation energy of −0.39 eV on Mo^{6+} and −0.34 eV on Mo^{5+}. Therefore, we only consider hops between Mo^{6+} ions.

As shown in Fig. 1, the possible polaron sites lead to five distinct oct–oct hops in $LiTM_2(PO_4)_3$, two distinct oct–oct hops in $Li_3TM_2(PO_4)_3$, two distinct oct–tet and four distinct tet–tet hops in $LiTi_2(VO_4)_3$ and in $LiGe_2(VO_4)_3$. For $LiTi_2(MoO_4)_3$ we

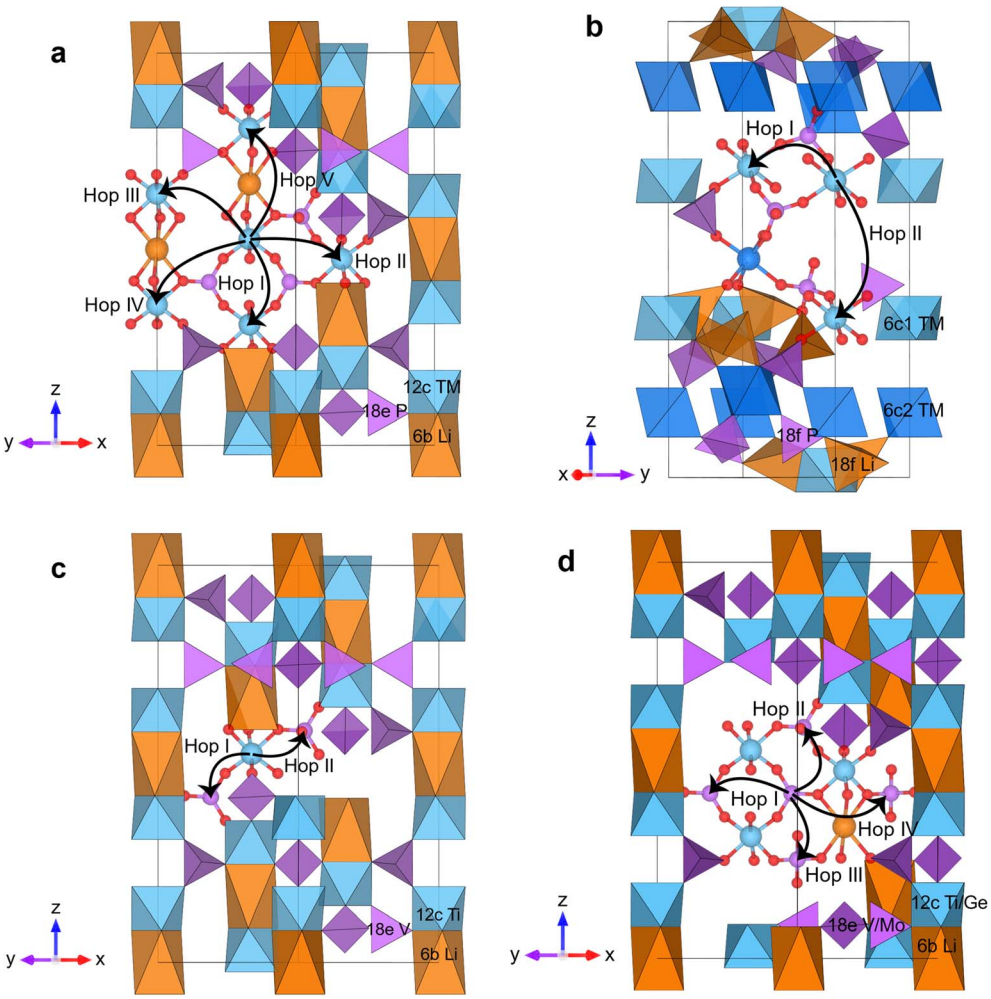

Fig. 1 Electron polaron hops of (a) oct–oct hopping in $LiTM_2(PO_4)_3$, TM = Ti/V/Cr/Mn/Fe; (b) oct–oct hopping in $Li_3TM_2(PO_4)_3$, TM = Ti/Cr/Fe; (c) oct–tet hopping in $LiTi_2(VO_4)_3$; and (d) tet–tet hopping in $LiTi_2(TMO_4)_3$, TM = V/Mo and $LiGe_2(VO_4)_3$. Only atoms near each constitutive hop are shown. The orange spheres denote Li atoms, the blue spheres denote atoms (TMs or Ge) in octahedral sites, the purple spheres denote atoms (P, V, or Mo) in tetrahedral sites, and the red spheres denote O atoms. All constitutive electron polaron hops are represented by the arrows from the center TM atom. For $Li_3TM_2(PO_4)_3$ in (b), the dark blue octahedra denote 6c2 sites which cannot accommodate polarons. The hops we consider for $LiTi_2(MoO_4)_3$ are the hop I and hop IV in (d).

Table 2 The first column gives the direction of the percolating paths. The second column gives the constitutive hops that create the percolating paths, and the last column gives the Wyckoff site involved. The //[001] and ⊥[001] direction correspond respectively to the direction parallel to and perpendicular to the z-axis in the Li-NASICON structure in Fig. 1

$LiTM_2(PO_4)_3$, TM = Ti,V,Cr,Mn,Fe Oct–oct hopping			$Li_3TM_2(PO_4)_3$, TM = Ti,Cr,Fe Oct–oct hopping		
Direction	Constitutive hop	Wyckoff site	Direction	Constitutive hop	Wyckoff site
//[001]	Hop I–Hop V	12c	//[001]	Hop I–Hop II	6c1
⊥[001]	Hop II	12c	⊥[001]	Hop I	6c1
⊥[001]	Hop III	12c			
⊥[001]	Hop IV	12c			
$LiTi_2(VO_4)_3$ Oct–tet hopping			$LiTi_2(VO_4)_3$ and $LiGe_2(VO_4)_3$ Tet–tet hopping		
Direction	Constitutive hop	Wyckoff site	Direction	Constitutive hop	Wyckoff site
//[001]	Hop II–Hop III	18e	⊥[001]	Hop I–Hop II	12c (Oct) and 18e (Tet)
⊥[001]	Hop I–Hop IV	18e			
⊥[001]	Hop IV	18e			
$LiTi_2(MoO_4)_3$ Tet–tet hopping					
Direction	Constitutive hop	Wyckoff site			
⊥[001]	Hop I–Hop IV	18e			

only considered two tet–tet hops through the Mo^{6+}/Mo^{5+} pair perpendicular to [001], as the other two hops parallel to [001] create Mo^{4+} ions. For $Li_3TM_2(PO_4)_3$, we only investigate the oct–oct polaronic transport as P^{5+} is unlikely to accommodate a polaron.

The possible hops join to form percolating conduction paths. In this study, we classify the percolating paths into two types: perpendicular to [001] or parallel to [001]. For $LiTi_2(MoO_4)_3$, we only consider percolating paths perpendicular to [001]. The oct–tet hopping in $LiTi_2(VO_4)_3$ only leads to a percolating path perpendicular to [001]. The directions of all percolating paths, possible hops, and the polaron Wyckoff site are listed in Table 2.

3.3. Rate-determining polaron hopping barriers of Li-NASICONs

To determine the rate-determining polaron hopping barriers in each compound, we first identify the hop with the highest barrier for each percolating conduction path. The path with the lowest maximum barrier is the preferential conduction path to realize percolating conduction, and the lowest maximum barrier is identified as the rate-determining hopping barrier for

Table 3 Electron polaron hopping barriers of the hops in Li-NASICONs. The rate-determining hopping barrier (in eV) of each Li-NASICON is highlighted by the bold number. For $LiTi_2(VO_4)_3$, two hopping barriers are highlighted as there are two hops with the same maximum barriers in the percolating conduction path

	Oct–oct hopping					Tet–tet hopping		
	$LiTi_2(PO_4)_3$	$LiV_2(PO_4)_3$	$LiCr_2(PO_4)_3$	$LiMn_2(PO_4)_3$	$LiFe_2(PO_4)_3$	$LiTi_2(VO_4)_3$	$LiGe_2(VO_4)_3$	$LiTi_2(MoO_4)_3$
Hop I	0.16	0.28	0.26	0.43	0.14	**0.40**	0.51	0.26
Hop II	**0.22**	**0.26**	0.23	0.36	0.12	0.39	0.54	—
Hop III	0.27	0.27	**0.19**	0.43	0.13	0.49	0.58	—
Hop IV	0.28	0.33	0.26	**0.35**	**0.09**	**0.40**	**0.52**	**0.29**
Hop V	0.30	0.38	0.33	0.47	0.25	—	—	—

	Oct–oct hopping			Oct–tet hopping
	$Li_3Ti_2(PO_4)_3$	$Li_3Cr_2(PO_4)_3$	$Li_3Fe_2(PO_4)_3$	$LiTi_2(VO_4)_3$
Hop I	**0.17**	**0.43**	**0.20**	0.41
Hop II	0.13	0.39	0.17	**0.45**

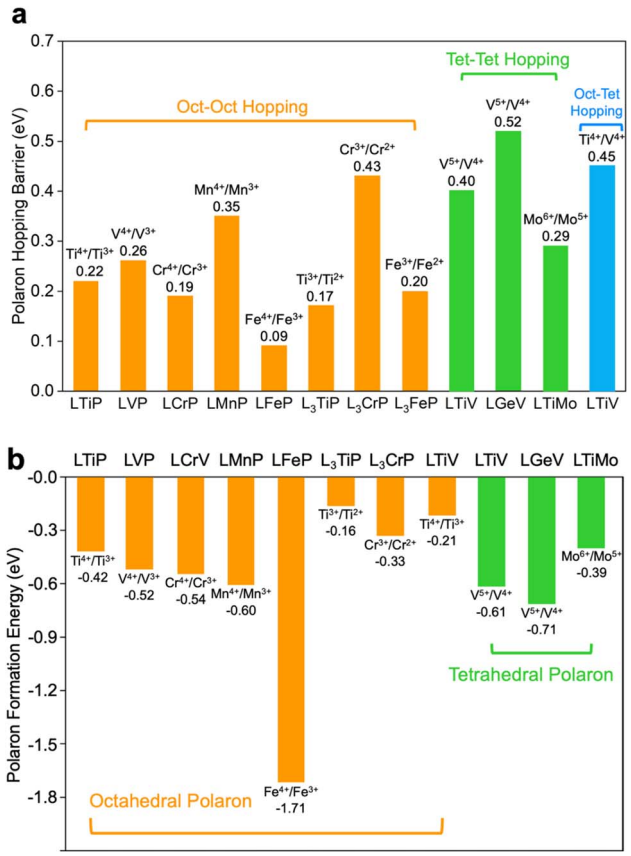

Fig. 2 (a) Rate-determining polaron hopping barriers of Li-NASICONs and (b) polaron formation energy in Li-NASICONs.

the polaronic conduction in a Li-NASICON. The barriers for all hops in each compound are shown in Table 3. For $LiTi_2(MoO_4)_3$, only the barriers of hop I and IV perpendicular to [001] with the Mo^{6+}/Mo^{5+} pair are calculated. The rate-determining hopping barriers are used to estimate the polaronic conductivity of Li-NASICONs.

The rate-determining hopping barriers of oct–oct hopping in different Li-NASICONs range from less than 0.1 eV to more than 0.4 eV, with the lowest barrier of 0.09 eV through the Fe^{4+}/Fe^{3+} pair and much higher hopping barriers of 0.35 and 0.43 eV through the Mn^{4+}/Mn^{3+} and Cr^{3+}/Cr^{2+} pairs, respectively. The oct–oct hopping through the Ti^{4+}/Ti^{3+}, V^{4+}/V^{3+}, Cr^{4+}/Cr^{3+}, Ti^{3+}/Ti^{2+}, and Fe^{3+}/Fe^{3+} have barriers between 0.15 and 0.3 eV. These results indicate element-dependent oct–oct polaron transport in Li-NASICONs. The tet–tet hopping also depends on the nature of the TM present on that site. Although hopping through the V^{5+}/V^{4+} pair has an energy barrier of more than 0.4 eV in $LiTi_2(VO_4)_3$ and $LiGe_2(VO_4)_3$, through the Mo^{6+}/Mo^{5+} pair in $LiTi_2(MoO_4)_3$ a lower barrier of 0.29 eV has to be crossed. In $LiTi_2(VO_4)_3$, the oct–tet hopping has a high barrier of 0.45 eV through the Ti^{4+}/V^{4+} pair. The rate-determining polaron hopping barriers for all Li-NASICONs are shown in Fig. 2a. All rate-determining hops occur along the percolating paths perpendicular to [001].

3.4. Polaronic conductivity in Li-NASICONs

We estimate the room-temperature polaronic conductivity of Li-NASICONs from the calculated rate-determining hopping barriers using the Marcus theory framework, which formulates the rate of charge-transfer across molecules or atoms in compounds.[76–78] In Marcus theory, a small polaron hopping is described by a parabolic free-energy curve for the polaron on each site, and their crossing point gives the hopping activation energy. When a polaron transfers from one site to another, its energy rises and reaches a maximum when the polaronic distortion is distributed between the two sites. At this crossing point, the polaron hopping rate depends on the tunneling probability. A tunneling probability close to identity indicates an adiabatic charge transfer, whereby a polaron hops to the final state once the lattice distortion reaches the transition-state configuration. In contrast, a limited tunneling probability results in a diabatic charge transfer, and the polaron may go back to the initial state even when the transition state has been reached. The tunneling probability is given by[78]

$$P_{\text{tunnel}} = 1 - \exp[-(V_e^2/h\upsilon_n)(\pi^3/\lambda k_B T)^{1/2}], \quad (1)$$

Table 4 Characteristic properties of polaronic conduction in Li-NASICONs. V_e denotes the electronic coupling, n denotes the polaron concentration evaluated as one polaron per unit cell given by 1/(cell volume), a denotes the hopping distance, E_a is the hopping barrier, and P_{tunnel} is the tunneling probability

	V_e (eV)	n (#/cm^3)	a (Å)	E_a (eV)	P_{tunnel}	Transfer type	Conductivity at 300 K (S cm^{-1})
$LiTi_2(PO_4)_3$	0.23	7.626×10^{20}	5.03	0.22	1	Adia; oct–oct	2.42×10^{-2}
$LiV_2(PO_4)_3$	0.38	7.863×10^{20}	4.99	0.26	1	Adia; oct–oct	5.24×10^{-3}
$LiCr_2(PO_4)_3$	0.30	8.067×10^{20}	5.37	0.19	1	Adia; oct–oct	9.31×10^{-2}
$LiMn_2(PO_4)_3$	0.33	8.229×10^{20}	5.85	0.35	1	Adia; oct–oct	2.32×10^{-4}
$LiFe_2(PO_4)_3$	0.13	8.430×10^{20}	5.85	0.09	1	Adia; oct–oct	5.51
$Li_3Ti_2(PO_4)_3$	0.20	7.171×10^{20}	4.89	0.17	1	Adia; oct–oct	1.49×10^{-1}
$Li_3Cr_2(PO_4)_3$	0.23	7.599×10^{20}	4.83	0.43	1	Adia; oct–oct	6.65×10^{-6}
$Li_3Fe_2(PO_4)_3$	0.18	7.405×10^{20}	4.86	0.20	1	Adia; oct–oct	4.75×10^{-2}
$LiTi_2(VO_4)_3$	0.41	6.650×10^{20}	3.43	0.45	1	Adia; oct–tet	1.35×10^{-6}
$LiTi_2(VO_4)_3$	0.50	6.650×10^{20}	4.51	0.40	1	Adia; tet–tet	1.62×10^{-5}
$LiGe_2(VO_4)_3$	0.30	6.994×10^{20}	5.54	0.52	1	Adia; tet–tet	2.48×10^{-7}
$LiTi_2(MoO_4)_3$	0.40	5.999×10^{20}	5.82	0.29	1	Adia; tet–tet	1.70×10^{-3}

where V_e is the electronic coupling between the initial and final state; h is Planck's constant; υ_n is the characteristic phonon vibrational frequency, which is on the order of 10^{13} Hz; λ is the reorganization energy; k_B is Boltzmann's constant; and T is the temperature in Kelvin. In a diabatic polaron transfer, the reorganization energy is approximated as $4 \times E_{diabatic}$, where $E_{diabatic}$ is the diabatic hopping barrier[78] and is evaluated as the sum of the hopping barrier and the charge transfer integral. The electronic coupling, V_{AB}, is estimated along the lines of the Mulliken–Hush formalism within Marcus theory.[79] In this formalism, ΔE_{12} is the energy difference between the polaronic bonding and antibonding states in the transition state during a hop and is related to the electronic coupling V_{AB}, as $V_{AB} = \frac{1}{2}\Delta E_{12}$.[80] Calculations of V_{AB} are conducted using the LOBSTER software,[81,82] which projects electron wavefunctions using local atomic orbital basis sets and reconstructs the atomic orbital-resolved bonding information between specific atomic pairs in a compound. The results for the calculated polaronic bonding and antibonding states are shown in Fig. S3.†

We estimate polaron hopping frequencies to obtain the diffusivities in Li-NASICONs. The adiabatic and diabatic polaron hopping frequencies are given by[78]

$$f_{adiabatic} = \upsilon_n \exp[-E_a/k_B T] \quad (2)$$

Table 5 Polaron hopping barriers, electronic coupling, tunneling probability and hopping types for all hops in Li-NASICONs. The rate-determining step for evaluating the polaronic conductivity of each Li-NASICON is marked by bold characters. The cutoff tunneling probability for diabatic/adiabatic hopping is arbitrarily set to 98%

		E_a (eV)	V_e (eV)	$P_{tunneling}$	Hopping type
$LiTi_2(PO_4)_3$	Hop I	0.16	0.28	1	Adiabatic
	Hop II	**0.22**	**0.23**	**1**	**Adiabatic**
	Hop III	0.27	0.13	1	Adiabatic
	Hop IV	0.28	0.13	1	Adiabatic
	Hop V	0.30	0.03	0.480	Diabatic
$LiV_2(PO_4)_3$	Hop I	0.28	0.25	1	Adiabatic
	Hop II	**0.26**	**0.38**	**1**	**Adiabatic**
	Hop III	0.27	0.23	1	Adiabatic
	Hop IV	0.33	0.18	1	Adiabatic
	Hop V	0.38	0.03	0.444	Diabatic
$LiCr_2(PO_4)_3$	Hop I	0.26	0.18	1	Adiabatic
	Hop II	0.23	0.40	1	Adiabatic
	Hop III	**0.19**	**0.30**	**1**	**Adiabatic**
	Hop IV	0.26	0.23	1	Adiabatic
	Hop V	0.33	0.03	0.466	Diabatic
$LiMn_2(PO_4)_3$	Hop I	0.43	0.13	1	Adiabatic
	Hop II	0.36	0.28	1	Adiabatic
	Hop III	0.43	0.18	1	Adiabatic
	Hop IV	**0.35**	**0.33**	**1**	**Adiabatic**
	Hop V	0.47	0.03	0.413	Diabatic
$LiFe_2(PO_4)_3$	Hop I	0.14	0.05	0.909	Diabatic
	Hop II	0.12	0.08	0.997	Adiabatic
	Hop III	0.13	0.05	0.915	Diabatic
	Hop IV	**0.09**	**0.13**	**1**	**Adiabatic**
	Hop V	0.25	0.05	0.852	Diabatic
$Li_3Ti_2(PO_4)_3$	**Hop I**	**0.17**	**0.20**	**1**	**Adiabatic**
	Hop II	0.13	0.03	0.610	Diabatic
$Li_3Cr_2(PO_4)_3$	**Hop I**	**0.43**	**0.23**	**1**	**Adiabatic**
	Hop II	0.39	0.03	0.440	Diabatic
$Li_3Fe_2(PO_4)_3$	**Hop I**	**0.20**	**0.18**	**1**	**Adiabatic**
	Hop II	0.17	0.03	0.569	Diabatic
$LiTi_2(VO_4)_3$ (oct–tet)	Hop I	0.41	0.51	1	Adiabatic
	Hop II	**0.45**	**0.41**	**1**	**Adiabatic**
$LiTi_2(VO_4)_3$ (tet–tet)	**Hop I**	**0.40**	**0.50**	**1**	**Adiabatic**
	Hop II	0.39	0.23	1	Adiabatic
	Hop III	0.49	0.18	1	Adiabatic
	Hop IV	**0.40**	**0.48**	**1**	**Adiabatic**
$LiGe_2(VO_4)_3$	Hop I	0.51	0.45	1	Adiabatic
	Hop II	0.54	0.23	1	Adiabatic
	Hop III	0.58	0.18	1	Adiabatic
	Hop IV	**0.52**	**0.30**	**1**	**Adiabatic**
$LiTi_2(MoO_4)_3$	Hop I	0.26	0.40	1	Adiabatic
	Hop IV	**0.29**	**0.40**	**1**	**Adiabatic**
$LiTi_2(VO_4)_{1/9}(PO_4)_{8/9}$	**Hop I**	**0.38**	**0.53**	**1**	**Adiabatic**
	Hop II	0.38	0.58	1	Adiabatic

$$f_{\text{diabatic}} = \left(4\pi^2/h\right) V_e{}^2 \left(1\Big/\sqrt{4\pi\lambda k_B T}\right) \times \exp\left[-\left(\Delta G^0 + \lambda\right)^2 \Big/ 4\lambda k_B T\right], \quad (3)$$

where ΔG^0 is the energy difference between polarons in the initial and final state. Herein, $Li_3Cr_2(PO_4)_3$ and $Li_3Fe_2(PO_4)_3$ have diabatic rate-determining hops as these hops involve polaron tunneling probability deviating from identity as shown in Table 4. The ΔG^0 is negligible as the initial and final TM site with a polaron are symmetrically equivalent. The diffusivity and polaron mobility are then expressed as:[78]

$$D = fa^2 g \text{ (diffusivity)} \quad (4)$$

$$u = eD/k_B T \text{ (charge mobility).} \quad (5)$$

Here, f is either the adiabatic or diabatic polaron hopping frequency, a is the hopping distance between two TM atoms, g is the available TM site near the initial polaronic site for hopping and is assumed to be 1 as the rate-determining hop contains only one available final TM site for a polaron, and e is the elementary charge. Polaronic conductivity is the product of polaron concentration (n), elementary charge (e), and mobility (u):

$$\sigma = neu. \quad (6)$$

Ultimately, for adiabatic and diabatic polaron hopping, the conductivity can be formulated as

$$\sigma_{\text{adiabatic}} = (ne^2 v_n a^2 g/k_B T) \times \exp[-E_a/k_B T] \quad (7)$$

$$\sigma_{\text{diabatic}} = \left(4\pi^2 ne^2 a^2 g/hk_B T\right)\sqrt{4\pi\lambda k_B T} \times \exp[-E_a/k_B T]. \quad (8)$$

All predicted characteristic properties of the rate-determining hops in Li-NASICONs are listed in Table 4.

Although the polaronic conductivity is determined by the hopping barrier and tunneling probability, for Li-NASICONs, most of the hops are adiabatic with tunneling probabilities of identity. Even the most diabatic hop, which is found in $LiMn_2(PO_4)_3$, has a tunneling probability of 0.41, suggesting a feasible polaron transfer when the transition state is reached, as shown in Table 5. Therefore, for Li-NASICONs the polaronic conductivity is mainly dominated by the hopping barrier and a percolating path with the lowest maximum barrier is the path with the highest polaronic conductivity. Amongst all Li-NASICONs in the current study, polaron transport *via* the Fe^{4+}/Fe^{3+} pair on octahedral sites in $LiFe_2(PO_4)_3$ has the highest calculated room-temperature conductivity of 5.51 S cm^{-1}, whereas the transport through the Cr^{3+}/Cr^{2+} pair on octahedral sites in $Li_3Cr_2(PO_4)_3$ and through the V^{5+}/V^{4+} pair on tetrahedral sites in $LiTi_2(VO_4)_3$ and $LiGe_2(VO_4)_3$ has much lower predicted room-temperature conductivity of 10^{-7} to 10^{-5} S cm^{-1}. The oct–tet polaron transport in $LiTi_2(VO_4)_3$ is also predicted to be poor (near 10^{-6} S cm^{-1}). All rate-determining hops of Li-NASICONs are adiabatic.

4. Discussion

Owing to the corner-sharing framework that alleviates the coulombic repulsion between Li ions and positively charged TM ions,[83] Li-NASICONs have low ionic migration barriers and high room-temperature ionic conductivities of 10^{-4} to 10^{-3} S cm^{-1}.[84,85] However, intrinsic wide band gaps (several eVs) and narrow bands prohibit band conduction in the structures.[85] For instance, $LiTi_2(PO_4)_3$ has a band gap of 2.50 eV (ref. 86) and a low room-temperature electronic conductivity of 10^{-8} S cm^{-1}.[87] To improve their electronic transport, attempts have been made to exploit mixed-valency in Li-NASICONs to generate localized charge carriers such that electronic conduction is activated *via* a polaron hopping mechanism. Specifically, Sharma and Dalvi[25] doped vanadium into $LiTi_2(PO_4)_3$ and $Li_{1.3}Al_{0.3}Ti_{1.7}(PO_4)_3$ to generate $LiTi_2(VO_4)_x(PO_4)_{3-x}$ and $Li_{1.3}Al_{0.3}Ti_{1.7}(VO_4)_x(PO_4)_{3-x}$ and improved its room-temperature electronic conductivity to 10^{-5} S cm^{-1}.

4.1. Polaronic conduction in $LiTi_2(VO_4)_x(PO_4)_{3-x}$

To validate our computational results, we compare the predicted hopping barrier and the room-temperature polaronic conductivity of $LiTi_2(VO_4)_x(PO_4)_{3-x}$ with published experimental results.[25] We replace two P atoms with V atoms in $LiTi_2(PO_4)_3$ to approximate the experimental composition of $LiTi_2(VO_4)_{0.3}(PO_4)_{2.7}$ (Fig. S5†). In this V-doped Li-NASICON, the polaron formation is more favorable on V atoms than on Ti atoms, as the charge only localizes on V atoms even when a structural distortion and an initialization of the Ti magnetic moment are imposed on a Ti–O_6 octahedron. The preferential localization of an electron polaron on a V atom in a tetrahedral site is consistent with the experimental observation of V^{5+}/V^{4+} pairs in the V-doped Li-NASICON. The computed tet–tet hopping barrier *via* the V^{5+}/V^{4+} pair is 0.38 eV, comparable but somewhat higher than the experimental hopping barrier of 0.20 eV. The computed room-temperature polaronic conductivity is 3.62×10^{-5} S cm^{-1}, in reasonable agreement with the experimental conductivity of 4.46×10^{-6} S cm^{-1}. In our calculations, the polaron concentration is fixed at one polaron per supercell containing 72 oxygen atoms.

4.2. Correlation between J–T distortion and rate-determining hopping barrier of oct–oct polaron transport in Li-NASICONs

We classify the oct–oct polaron transport into three classes depending on the presence of any Jahn–Teller (J–T) activity with or without the electron polaron present: only the state with polaron is J–T active (Class 1: Mn^{4+}/Mn^{3+} and Cr^{3+}/Cr^{2+}); both the polaronic and pristine state of the TMs are J–T inactive (Class 2: Ti^{4+}/Ti^{3+}, V^{4+}/V^{3+}, Cr^{4+}/Cr^{3+}, Ti^{3+}/Ti^{2+} and Fe^{3+}/Fe^{2+}); and only the state without the polaron is J–T active (Class 3: Fe^{4+}/Fe^{3+}). We note that only cations with a doublet degeneracy in the e_g band (Exe J–T coupling) involving a static J–T distortion are classified as J–T active, whereas cations with either a triplet degeneracy in the t_{2g} band (T_x(t + e) coupling) involving a dynamic J–T effect, or cations with no degeneracy, are

classified as J–T inactive. For Class 1, the J–T distortion is stabilized by the electron polaron formation and results in a relatively high hopping barrier as the lattice distortion that must be migrated is largely caused by the J–T coupling with the polaron. This leads to low polaronic conduction in $LiMn_2(PO_4)_3$ and $Li_3Cr_2(PO_4)_3$. For Class 2, no J–T distortion is involved during polaron hopping, resulting in lower hopping barriers than those of class one. In Class 3, the J–T distortion vanishes upon the formation of an electron polaron leading to a lower lattice distortion, while the TM sites without the extra electron are "pre-distorted" and possess multiple degrees of freedom by which they can distort at low cost in energy (*i.e.*, the J–T modes).[88] Hence, the polaronic conductivity in $LiFe_2(PO_4)_3$ is the highest with a very low barrier of 0.09 eV. This obvious correlation between hopping barriers and J–T distortion in Li-NASICONs reflects the adiabatic nature of polaron transport, which is phonon-assisted and dominated by the transport of the lattice distortion. The TM–O bond lengths of the J–T active species are shown in Table S1.†

With the assumption that polaron transport can be approximated as adiabatic hopping at room temperature in most oxides,[69,89,90] other materials involving TM–O_6 octahedra might also exhibit a correlation between high conductivity and J–T distortion in the non-polaronic TM ion. For instance, in olivine $LiMPO_4$ structured phosphates, the hole polaron hopping barrier *via* the Mn^{2+}/Mn^{3+} pair is more than 0.3 eV, higher than those through the Fe^{2+}/Fe^{3+} and Co^{2+}/Co^{3+} pairs with no J–T distortion during hopping,[59] consistent with the fact that Mn^{3+} is J–T active. In addition, both the hole polaron hopping through the Co^{3+}/Co^{4+} pair and the electron polaron hopping through the Co^{3+}/Co^{2+} pair involve no J–T distortion in $LiCoO_2$ (ref. 60) and have energy barriers roughly between 0.1 and 0.3 eV, which are similar to the hopping barriers in class two. Furthermore, the electron polaron transport through the Mo^{6+}/Mo^{5+} J–T inactive pair in MoO_3 ranges from 0.11 to 0.35 eV,[61] similar to the hopping barriers in class two. Notably, the electron polaron hopping barrier through the Mn^{3+}/Mn^{2+} pair in $MnPO_4$ is only two-thirds of the hole polaron hopping barrier through the Mn^{2+}/Mn^{3+} pair in $LiMnPO_4$.[62] The applicability of J–T distortion-correlated polaron hopping barriers to other oxides of TMs underpins the 3d electronic configuration as an indicator for polaronic conduction. Despite the hopping barriers of the oct–oct polaronic transport being quite different among various mixed-valency pairs, a majority of Li-NASICONs have predicted room-temperature polaronic conductivity above 10^{-4} S cm^{-1}, including those with the Ti^{4+}/Ti^{3+}, Ti^{3+}/Ti^{2+}, V^{4+}/V^{3+}, Cr^{4+}/Cr^{3+}, Fe^{4+}/Fe^{3+}, and Fe^{3+}/Fe^{2+} mixed-valency pairs. Polaronic conduction through the oct–oct pathway in Li-NASICONs may open up the possibility of Li-NASICON mixed ionic electronic conductors.

Previous study on polaron hopping in AgCl compound found that the hopping barrier depends on the orientation of the J–T axis in the octahedra.[91] To investigate whether the orientation of the J–T axis influences the polaron hopping barrier in Li-NASICONs, we examine whether polaronic states can be stabilized along all three principal axes. We reorient the elongated axis of the original extrinsic J–T distorted octahedron of Mn^{3+} and Cr^{2+} along the other two principal axes and then perform geometry optimizations. Our results show that, in both Mn^{3+} and Cr^{2+} octahedra, the elongated axis reverts back to the original principal axis, indicating that J–T distortion is only stable along a single principal axis in Li-NASICONs. This finding rules out the possibility that the polaron hops by first changing direction of the JT axis and then hopping.

4.3. The effect of the Li charge state on polaron hopping in Li-NASICONs

Another factor that may contribute to the oct–oct polaron transport in the Ti-based Li-NASICONs is the amount of Li present in the NASICON. The additional Li ions in $Li_3Ti_2(PO_4)_3$ introduce attractive coulombic interactions with the polaron during a hop, potentially leading to a smoother hopping energy landscape and a lower hopping barrier. This effect is reflected in the two hopping barriers of 0.13 eV and 0.17 eV in $Li_3Ti_2(PO_4)_3$ compared to the hopping barriers in $LiTi_2(PO_4)_3$ which are mostly above 0.2 eV as shown in the Table 3. In contrast, for Cr-based NASICONs, although the additional Li^+ ions in $Li_3Cr_2(PO_4)_3$ could facilitate polaron hopping, their effect may be overpowered by the J–T active Cr^{2+} upon polaron formation resulting in a higher barrier. Hence, unlike in Ti-based NASICONs where increasing the Li content lowers the hopping barriers, $Li_3Cr_2(PO_4)_3$ has higher hopping barriers than in $LiCr_2(PO_4)_3$, as shown in the Table 3.

4.4. Oct–tet and tet–tet polaron transport in Li-NASICONs

Oct–tet polaron transport is kinetically less favorable than oct–oct polaron transport in the only compound for which we evaluate this because of the difference in the polaron formation energy on a Ti and V atom in $LiTi_2(VO_4)_3$. Although a polaron on Ti has a formation energy of −0.21 eV, it is more stable on V with a formation energy of −0.61 eV, which leads to an asymmetric hopping energy landscape that creates a high barrier of 0.45 eV, as shown in Fig. 3. Oct–tet polaron hopping may also have high barriers in other systems due to the difference in the polaron formation energy in the different coordinated environments. Similar results were reported in a previous study on oct–tet electron polaron hopping in Co_3O_4.[92]

As fewer TM elements (V and Mo) have been reported to occupy tetrahedral sites in Li-NASICONs, tet–tet polaron

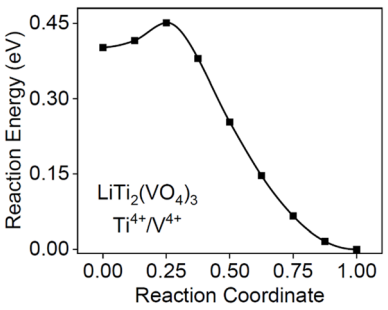

Fig. 3 Asymmetric polaron hopping energy curve of oct–tet polaron transport in $LiTi_2(VO_4)_3$.

hopping may be of less practical importance for application in MIECs. Nonetheless, the room-temperature polaronic conductivity *via* the Mo^{6+}/Mo^{5+} pair on tetrahedral sites in $LiTi_2(MoO_4)_3$ is predicted to be on the order of 10^{-3} S cm^{-1}, comparable to the room-temperature ionic conductivities in Li-NASICONs reported in previous studies.[93–95] This result indicates that molybdenum-based Li-NASICONs may also exhibit efficient electronic conductivity *via* polaronic conduction.

4.5. The effect of lattice volume and polaronic orbital overlap on polaronic conduction in Li-NASICONs

Aside from the J–T distortion, other factors have also been proposed to account for the different hopping barriers in a compound. For instance, Kweon *et al.*[52] and Moradabadi *et al.*[90] independently pointed at an increase in the polaron hopping barrier as a result of lattice expansion for $BiVO_4$ and $LiCoO_2$, respectively. In our study, we also find a similar trend in the hopping barriers of $LiTi_2(PO_4)_3$ and $LiGe_2(VO_4)_3$, as shown in Fig. 4. Lattice expansions elongate the hopping distance between two TM atoms, which is accompanied by the increase in the hopping barrier, consistent with the previous studies. However, the volume changes arising from the chemistry differences in Li-NASICONs cannot explain the barrier variation seen with chemistry. Fig. 5 shows the oct–oct hopping barrier as a function of the volume of each $LiTM_2(PO_4)_3$ unit cell. Although the lattice volume of Li-NASICONs monotonically increases from Ti to Fe, the hopping barriers of oct–oct polaronic transport *via* their +4/+3 mixed-valency TMs show no such monotonic change.

Another possible factor reported by Garcia-Lastra *et al.*[96] to affect polaron hopping barrier is the extent of polaronic orbital overlap. These authors found that both hole polaron and electron polaron hopping barriers exhibit differences along different hopping directions in Li_2O_2 stemming from the different extent of polaronic orbital overlap in the transition states. Nevertheless, these differences in hopping barriers were found to be less than 0.1 eV in Li_2O_2 and may have limited effect on the polaronic transport. The polaronic orbital overlap is quantified by the integration of the projected crystal orbital Hamilton population (pCOHP) of the polaronic state with respect to energy up to the highest occupied state (the Fermi level);[97] namely, the integrated projected crystal orbital Hamilton population (IpCOHP). We compute the IpCOHP of the

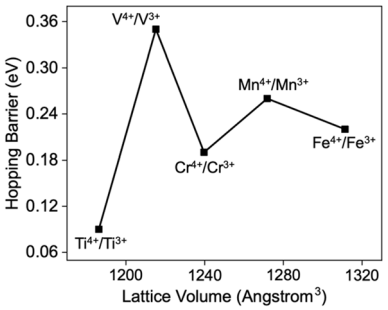

Fig. 5 Oct–oct polaron hopping barrier as a function of the lattice volume of $LiTM_2(PO_4)_3$, TM = Ti, V, Cr, Mn, and Fe.

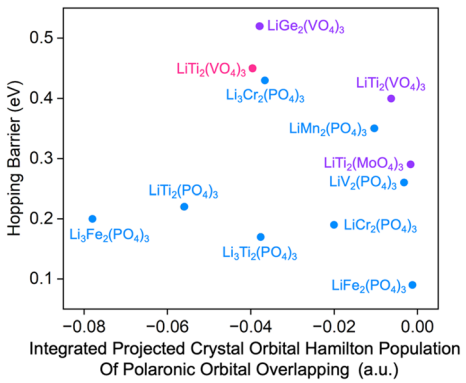

Fig. 6 Polaron hopping barrier as a function of the polaronic orbital overlap between the 3d orbitals of two TMs participating in the rate-determining hop in the transition state of Li-NASICONs. The blue data points denote oct–oct hopping, the pink data point denotes oct–tet hopping, and the purple data points denote tet–tet hopping.

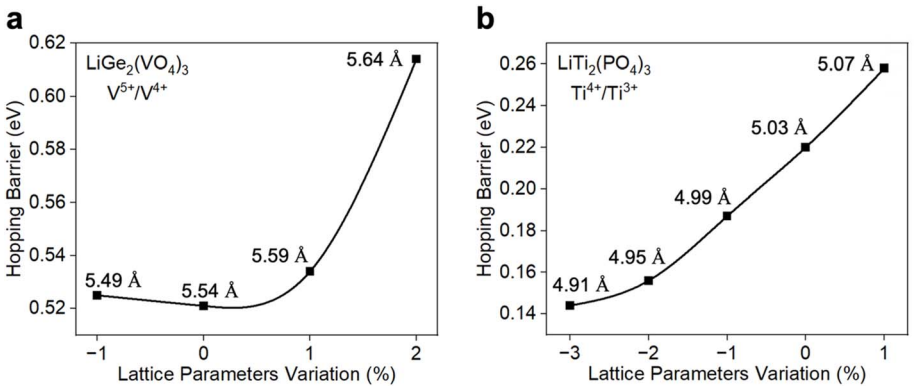

Fig. 4 Polaron hopping barrier *versus* lattice parameter variation of (a) $LiGe_2(VO_4)_3$ and (b) $LiTi_2(PO_4)_3$. The lattice parameter variation is the percentage of the homogeneous compression or elongation of the lattice parameters in all three dimensions, *i.e.*, −1% denotes compressing all three lattice parameters by 1%; 1% denotes elongating all three lattice parameters by 1%. Numbers near squares denote the polaron hopping distance.

polaronic 3d orbitals of two TM atoms participating in the rate-determining hop in the transition states of various Li-NASICONs, and plot them in Fig. 6. There appears to be no correlation between the overlaps and the hopping barriers.

5. Conclusion

We examine polaronic conduction in Li-NASICONs using first-principles calculations and demonstrate that significantly enhanced electronic conductivity may be achieved from polaron hopping if a high enough carrier concentration can be generated. Polaronic conductivities through the Ti^{4+}/Ti^{3+}, Ti^{3+}/Ti^{2+}, V^{4+}/V^{3+}, Cr^{4+}/Cr^{3+}, Fe^{4+}/Fe^{3+}, Fe^{3+}/Fe^{2+}, and Mo^{6+}/Mo^{5+} pairs are predicted to be over 10^{-4} S cm^{-1} at room temperature, with the highest conductivity of 5.51 S cm^{-1} achieved through the Fe^{4+}/Fe^{3+} pair in $LiFe_2(PO_4)_3$. Our calculations indicate that in Li-NASICONs, the hopping barrier of oct–oct polaron transport is correlated with the J–T distortion associated with polaron formation, whereas the lattice volume and the polaronic orbital overlap have minor effects on polaronic conduction. Our understanding of polaronic conduction in Li-NASICONs may assist in identifying effective strategies to develop Li-NASICON MIECs for electrochemical energy storage devices.

Data availability

The authors confirm that the data supporting the findings of this study are available within the article and its ESI.†

Conflicts of interest

The authors declare no conflict of interest.

Acknowledgements

This work is supported by the Samsung Advanced Institute of Technology (SAIT). The computational analysis is performed using computational resources sponsored by the Department of Energy's Office of Energy Efficiency and Renewable Energy located at the National Renewable Energy Laboratory (NREL) under the *saepssic* and *ahlssic* allocations. Computational resources are also provided by the Advanced Cyberinfrastructure Coordination Ecosystem: Services & Support (ACCESS) program, which is supported by National Science Foundation grants #2138259, #2138286, #2138307, #2137603, and #2138296. K. Jun gratefully acknowledges support from the Kwanjeong Educational Foundation scholarship.

References

1 Y. Kyungho, K. JungJoon, S. WonMo, L. MyeongHwan and K. Kisuk, Investigation on the interface between $Li_{10}GeP_2S_{12}$ electrolyte and carbon conductive agents in all solid-state lithium battery, *Sci. Rep.*, 2018, **8**, 10366.
2 X. Yihan, W. Yan, B. ShouHang, K. JaeChul, J. M. Lincoln and G. Ceder, Understanding interface stability in solid-state batteries, *Nat. Rev. Mater.*, 2020, **5**, 105–126.
3 F. Li, T. Zhang and H. Zhou, Challenges of non-aqueous Li-O_2 batteries: electrolytes, catalysts, and anodes, *Energy Environ. Sci.*, 2013, **6**, 1125–1141.
4 B. M. Gallant, *et al.*, Chemical and Morphological Changes of Li-O_2 Battery Electrodes upon Cycling, *J. Phys. Chem. C*, 2012, **116**, 20800–20805.
5 M. M. O. Thotiyl, S. A. Freunberger, Z. Peng and P. G. Bruce, The Carbon Electrode in Nonaqueous Li-O_2 Cells, *J. Am. Chem. Soc.*, 2013, **135**, 494–500.
6 B. D. McCloskey, *et al.*, Twin Problems of Interfacial Carbonate Formation in Nonaqueous Li-O_2 Batteries, *J. Phys. Chem. Lett.*, 2012, **3**, 997–1001.
7 D. Cao, S. Zhang, F. Yu, Y. Wu and Y. Chen, Carbon-Free Cathode Materials for Li-O_2 Batteries, *Batteries Supercaps*, 2019, **2**, 428–439.
8 Z. Peng, S. A. Freunberger, Y. Chen and P. G. Bruce, A Reversible and Higher-Rate Li-O_2 Battery, *Science*, 2012, **337**, 563–566.
9 W. Luo, *et al.*, Binder-Free and Carbon-Free 3D Porous Air Electrode for Li-O_2 Batteries with High Efficiency, High Capacity, and Long Life, *Small*, 2016, **12**, 3031–3038.
10 F. Li, *et al.*, Li-O_2 Battery Based on Highly Efficient Sb-Doped Tin Oxide Supported Ru Nanoparticles, *Adv. Mater.*, 2014, **26**, 4659–4664.
11 F. Li, *et al.*, Ru/ITO: A Carbon-Free Cathode for Nonaqueous Li-O_2 Battery, *Nano Lett.*, 2013, **13**, 4702–4707.
12 J. Kang, *et al.*, Breathable Carbon-Free Electrode: Black TiO_2 with Hierarchically Ordered Porous Structure for Stable Li-O_2 Battery, *Adv. Energy Mater.*, 2017, **7**, 1700814.
13 G. Zhao, R. Mo, B. Wang, L. Zhang and K. Sun, Enhanced Cyclability of Li-O_2 Batteries Based on TiO_2 Supported Cathodes with No Carbon or Binder, *Chem. Mater.*, 2014, **26**, 2551–2556.
14 M. M. O. Thotiyl, *et al.*, A stable cathode for the aprotic Li-O_2 battery, *Nat. Mater.*, 2013, **12**, 1050–1056.
15 Y. Chang, *et al.*, A Carbon- and Binder-Free Nanostructured Cathode for High-Performance Nonaqueous Li-O_2 Battery, *Adv. Sci.*, 2015, **2**, 1500092.
16 J. Cheng, *et al.*, Perovskite $La_{0.6}Sr_{0.4}Co_{0.2}Fe_{0.8}O_3$ as an effective electrocatalyst for non-aqueous lithium air batteries, *Electrochim. Acta*, 2016, **191**, 106–115.
17 Q. Xu, *et al.*, $Ba_{0.9}Co_{0.7}Fe_{0.2}Nb_{0.1}O_{3-\delta}$ Perovskite as Oxygen Electrode Catalyst for Rechargeable Li-Oxygen Batteries, *Electrochim. Acta*, 2016, **191**, 577–585.
18 Y. Liu, *et al.*, Fabrication and Performance of All-Solid-State Li-Air Battery with SWCNTs/LAGP Cathode, *ACS Appl. Mater. Interfaces*, 2015, **7**, 17307–17310.
19 X. B. Zhu, T. S. Zhao, Z. H. Wei, P. Tan and G. Zhao, A novel solid-state Li-O_2 battery with an integrated electrolyte and cathode structure, *Energy Environ. Sci.*, 2015, **8**, 2782–2790.
20 H. T. T. Le, *et al.*, Highly efficient and stable solid-state Li-O_2 batteries using a perovskite solid electrolyte, *J. Mater. Chem. A*, 2019, **7**, 3150–3160.
21 X. Chi, *et al.*, A highly stable and flexible zeolite electrolyte solid-state Li-air battery, *Nature*, 2021, **592**, 551–557.
22 S. B. Ma, *et al.*, Mixed Ionic–Electronic Conductor of Perovskite $Li_xLa_yMO_{3-\delta}$ toward Carbon-Free Cathode for

Reversible Lithium-Air Batteries, *Adv. Energy Mater.*, 2020, **10**, 2001767.
23 M. Kim, *et al.*, Carbon-free high-performance cathode for solid-state Li-O_2 battery, *Sci. Adv.*, 2022, **8**, eabm8584.
24 Z. Jin, *et al.*, Garnet-type solid-state mixed ionic and electronic conductor, *Energy Storage Mater.*, 2023, **59**, 102788.
25 N. Sharma and A. Dalvi, Vanadium substituted Li^+-NASICON systems: Tailoring electronic conductivity for electrode applications, *J. Alloys Compd.*, 2021, **861**, 157954.
26 Q. Bai, Y. Zhu, X. He, E. Wachsman and Y. Mo, First principles hybrid functional study of small polarons in doped $SrCeO_3$ perovskite: towards computation design of materials with tailored polaron, *Ionics*, 2018, **24**, 1139–1151.
27 C. E. Schwarz, R. S. Saravanan, N. M. Borodin, Y. Liu, E. D. Wachsman and Y. Mo, Polaron-Based Electronic Conduction in Mixed Ionic-Electronic Conducting Lithium Garnets, *ACS Energy Lett.*, 2024, **9**(11), 5334–5340.
28 K. Zhang, *et al.*, Molybdenum-based NASICON $Li_2M_2(MoO_4)_3$ (M = Zn, Cu): Understanding structural evolution and lithium storage mechanism, *J. Alloys Compd.*, 2022, **890**, 161884.
29 K. Feng, F. Wang, H. Zhang, X. Li and H. Zhang, $Li_3Cr(MoO_4)_3$: a NASICON-type high specific capacity cathode material for lithium ion batteries, *J. Mater. Chem. A*, 2018, **6**, 19107–19112.
30 S. R. S. Prabaharan, A. Fauzi, M. S. Michael and K. M. Begam, New NASICON-type $Li_2Ni_2(MoO_4)_3$ as a positive electrode material for rechargeable lithium batteries, *Solid State Ionics*, 2004, **171**, 157–165.
31 C. Franchini, M. Reticcioli, M. Setvin and U. Diebold, Polarons in materials, *Nat. Rev. Mater.*, 2021, **6**, 560–586.
32 P. Huang and E. A. Carter, Advances in Correlated Electronic Structure Methods for Solids, Surfaces, and Nanostructures, *Annu. Rev. Phys. Chem.*, 2008, **59**, 261–290.
33 G. Pacchioni, Modeling doped and defective oxides in catalysis with density functional theory methods: Room for improvements, *J. Chem. Phys.*, 2008, **128**, 182505.
34 M. V. Ganduglia-Pirovano, A. Hofmann and J. Sauer, Oxygen vacancies in transition metal and rare earth oxides: Current state of understanding and remaining challenges, *Surf. Sci. Rep.*, 2007, **62**, 219–270.
35 A. I. Liechtenstein, V. I. Anisimov and J. Zaanen, Density-functional theory and strong interactions: Orbital ordering in Mott-Hubbard insulators, *Phys. Rev. B: Condens. Matter Mater. Phys.*, 1995, **52**, R5467–R5470.
36 S. L. Dudarev, G. A. Botton, S. Y. Savrasov, C. J. Humphreys and A. P. Sutton, Electron-energy-loss spectra and the structural stability of nickel oxide: An LSDA+U study, *Phys. Rev. B: Condens. Matter Mater. Phys.*, 1998, **57**, 1505–1509.
37 V. I. Anisimov, F. Aryasetiawan and A. I. Lichtenstein, First-principles calculations of the electronic structure and spectra of strongly correlated systems: the LDA+ U method, *J. Phys.: Condens. Matter*, 1997, **9**, 767.
38 M. Setvin, *et al.*, Direct View at Excess Electrons in TiO_2 Rutile and Anatase, *Phys. Rev. Lett.*, 2014, **113**, 086402.
39 T. D. Pham and N. A. Deskins, Efficient Method for Modeling Polarons Using Electronic Structure Methods, *J. Chem. Theory Comput.*, 2020, **16**, 5264–5278.
40 P. Deák, B. Aradi and T. Frauenheim, Polaronic effects in TiO_2 calculated by the HSE06 hybrid functional: Dopant passivation by carrier self-trapping, *Phys. Rev. B: Condens. Matter Mater. Phys.*, 2011, **83**, 155207.
41 E. Finazzi, C. D. Valentin, G. Pacchioni and A. Selloni, Excess electron states in reduced bulk anatase TiO_2: Comparison of standard GGA, GGA+U, and hybrid DFT calculations, *J. Chem. Phys.*, 2008, **129**, 154113.
42 J. Heyd, G. E. Scuseria and M. Ernzerhof, Hybrid functionals based on a screened Coulomb potential, *J. Chem. Phys.*, 2003, **118**, 8207–8215.
43 G. Kresse and J. Furthmüller, Efficiency of ab-initio total energy calculations for metals and semiconductors using a plane-wave basis set, *Comput. Mater. Sci.*, 1996, **6**, 15–50.
44 G. Kresse and J. Furthmüller, Efficient iterative schemes for ab initio total-energy calculations using a plane-wave basis set, *Phys. Rev. B: Condens. Matter Mater. Phys.*, 1996, **54**, 11169–11186.
45 G. Kresse and J. Hafner, Ab initio molecular dynamics for liquid metals, *Phys. Rev. B: Condens. Matter Mater. Phys.*, 1993, **47**, 558–561.
46 S. P. Ong, *et al.*, Python Materials Genomics (pymatgen): A robust, open-source python library for materials analysis, *Comput. Mater. Sci.*, 2013, **68**, 314–319.
47 D. M. Ramo, A. L. Shluger, J. L. Gavartin and G. Bersuker, Theoretical Prediction of Intrinsic Self-Trapping of Electrons and Holes in Monoclinic HfO_2, *Phys. Rev. Lett.*, 2007, **99**, 155504.
48 Z. Wang, C. Brock, A. Matt and K. H. Bevan, Implications of the DFT+U method on polaron properties in energy materials, *Phys. Rev. B*, 2017, **96**, 125150.
49 T. Shibuya, K. Yasuoka, S. Mirbt and B. Sanyal, A systematic study of polarons due to oxygen vacancy formation at the rutile TiO_2(110) surface by GGA + U and HSE06 methods, *J. Phys.: Condens. Matter*, 2012, **24**, 435504.
50 S. Chrétien and H. Metiu, Electronic Structure of Partially Reduced Rutile TiO_2(110) Surface: Where Are the Unpaired Electrons Located?, *J. Phys. Chem. C*, 2011, **115**, 4696–4705.
51 T. Liu, Q. Zhao, C. Li, Y. Lyu and M. Dupuis, Photocatalytic Facet Selectivity in $BiVO_4$ Nanoparticles: Polaron Electronic Structure and Thermodynamic Stability Considerations for Photocatalysis, *J. Phys. Chem. C*, 2019, **123**, 20142–20151.
52 K. E. Kweon, G. S. Hwang, J. Kim, S. Kim and S. Kim, Electron small polarons and their transport in bismuth vanadate: a first principles study, *Phys. Chem. Chem. Phys.*, 2014, **17**, 256–260.
53 R. Defrance, B. Sklénard, M. Guillaumont, J. Li and M. Freyss, Ab initio study of electron mobility in V_2O_5 via polaron hopping, *Solid-State Electron.*, 2022, **198**, 108455.
54 A. R. Elmaslmane, M. B. Watkins and K. P. McKenna, First-Principles Modeling of Polaron Formation in TiO_2 Polymorphs, *J. Chem. Theory Comput.*, 2018, **14**, 3740–3751.

55 H. J. Monkhorst and J. D. Pack, Special points for Brillouin-zone integrations, *Phys. Rev. B: Condens. Matter Mater. Phys.*, 1976, **13**, 5188–5192.
56 J. J. Plata, A. M. Márquez and J. F. Sanz, Electron Mobility via Polaron Hopping in Bulk Ceria: A First-Principles Study, *J. Phys. Chem. C*, 2013, **117**, 14502–14509.
57 C. W. M. Castleton, A. Lee and J. Kullgren, Benchmarking Density Functional Theory Functionals for Polarons in Oxides: Properties of CeO_2, *J. Phys. Chem. C*, 2019, **123**, 5164–5175.
58 S. P. Ong, Y. Mo and G. Ceder, Low hole polaron migration barrier in lithium peroxide, *Phys. Rev. B: Condens. Matter Mater. Phys.*, 2012, **85**, 081105.
59 M. D. Johannes, K. Hoang, J. L. Allen and K. Gaskell, Hole polaron formation and migration in olivine phosphate materials, *Phys. Rev. B: Condens. Matter Mater. Phys.*, 2012, **85**, 115106.
60 K. Hoang and M. D. Johannes, Defect chemistry in layered transition-metal oxides from screened hybrid density functional calculations, *J. Mater. Chem. A*, 2014, **2**, 5224–5235.
61 H. Ding, *et al.*, Computational Investigation of Electron Small Polarons in α-MoO_3, *J. Phys. Chem. C*, 2014, **118**, 15565–15572.
62 S. P. Ong, V. L. Chevrier and G. Ceder, Comparison of small polaron migration and phase separation in olivine LiMnPO4 and $LiFePO_4$ using hybrid density functional theory, *Phys. Rev. B: Condens. Matter Mater. Phys.*, 2011, **83**, 075112.
63 A. B. Bykov, *et al.*, Superionic conductors $Li_3M_2(PO_4)_3$ (M = Fe, Sc, Cr): Synthesis, structure and electrophysical properties, *Solid State Ionics*, 1990, **38**, 31–52.
64 M. Catti, S. Stramare and R. Ibberson, Lithium location in NASICON-type Li+ conductors by neutron diffraction. I. Triclinic α′-$LiZr_2(PO_4)_3$, *Solid State Ionics*, 1999, **123**, 173–180.
65 F. Sudreau, D. Petit and J. P. Boilot, Dimorphism, phase transitions, and transport properties in $LiZr_2(PO_4)_3$, *J. Solid State Chem.*, 1989, **83**, 78–90.
66 N. Anantharamulu, *et al.*, A wide-ranging review on Nasicon type materials, *J. Mater. Sci.*, 2011, **46**, 2821–2837.
67 M. Ménétrier, I. Saadoune, S. Levasseur and C. Delmas, The insulator-metal transition upon lithium deintercalation from $LiCoO_2$: electronic properties and 7Li NMR study, *J. Mater. Chem.*, 1999, **9**, 1135–1140.
68 C. A. Marianetti, G. Kotliar and G. Ceder, A first-order Mott transition in Li_xCoO_2, *Nat. Mater.*, 2004, **3**, 627–631.
69 J. Kaur, M. L. H. Chandrappa, C. Chen and S. P. Ong, Polaron-induced metal-to-insulator transition in vanadium oxides from density functional theory calculations, *Phys. Rev. B*, 2023, **107**, 125162.
70 A. Jain, *et al.*, Commentary: The Materials Project: A materials genome approach to accelerating materials innovation, *APL Mater.*, 2013, **1**, 011002.
71 Y. Xiao, Y. Wang, S. H. Bo, J. C. Kim, L. J. Miara and G. Ceder, Understanding interface stability in solid-state batteries, *Nat. Rev. Mater.*, 2020, **5**, 105–126.
72 Y. Zhu, X. He and Y. Mo, First principles study on electrochemical and chemical stability of solid electrolyte–electrode interfaces in all-solid-state Li-ion batteries, *J. Mater. Chem. A*, 2016, **4**, 3253–3266.
73 W. D. Richards, L. J. Miara, Y. Wang, J. C. Kim and G. Ceder, Interface Stability in Solid-State Batteries, *Chem. Mater.*, 2015, **28**, 266–273.
74 A. Manthiram and J. B. Goodenough, Lithium Insertion into $Fe_2(MO_4)_3$ Frameworks: Comparison of M = W with M = Mo, *J. Solid State Chem.*, 1987, **71**, 349–360.
75 D. MiKhailova, *et al.*, $Li_3V(MoO_4)_3$: A New Material for Both Li Extraction and Insertion, *Chem. Mater.*, 2010, **22**, 3165–3173.
76 R. A. Marcus and N. Sutin, Electron transfers in chemistry and biology, *Biochim. Biophys. Acta, Rev. Bioenerg.*, 1985, **811**, 265–322.
77 R. A. Marcus, Electron transfer reactions in chemistry. Theory and experiment, *Rev. Mod. Phys.*, 1993, **65**, 599–610.
78 N. A. Deskins and M. Dupuis, Electron transport via polaron hopping in bulk TiO_2: A density functional theory characterization, *Phys. Rev. B: Condens. Matter Mater. Phys.*, 2007, **75**, 195212.
79 J. R. Reimers and N. S. Hush, Electronic Properties of Transition-Metal Complexes Determined from Electroabsorption Mononuclear Complexes of Ruthenlum(II), *J. Phys. Chem.*, 1991, **95**, 9773–9781.
80 N. Adelstein, J. B. Neaton, M. Asta and L. C. D. Jonghe, Density functional theory based calculation of small-polaron mobility in hematite, *Phys. Rev. B: Condens. Matter Mater. Phys.*, 2014, **89**, 245115.
81 R. Nelson, *et al.*, LOBSTER: Local orbital projections, atomic charges, and chemical-bonding analysis from projector-augmented-wave-based density-functional theory, *J. Comput. Chem.*, 2020, **41**, 1931–1940.
82 S. Maintz, V. L. Deringer, A. L. Tchougréeff and R. Dronskowski, LOBSTER: A tool to extract chemical bonding from plane-wave based DFT, *J. Comput. Chem.*, 2016, **37**, 1030–1035.
83 K. Jun, *et al.*, Lithium superionic conductors with corner-sharing frameworks, *Nat. Mater.*, 2022, **21**, 924–931.
84 B. Lang, B. Ziebarth and C. Elsässer, Lithium Ion Conduction in $LiTi_2(PO_4)_3$ and Related Compounds Based on the NASICON Structure: A First-Principles Study, *Chem. Mater.*, 2015, **27**, 5040–5048.
85 X. Zhao, *et al.*, Computational screening and first-principles investigations of NASICON-type $Li_xM_2(PO_4)_3$ as solid electrolytes for Li batteries, *J. Mater. Chem. A*, 2018, **6**, 2625–2631.
86 H. Wang, *et al.*, Rational design and synthesis of $LiTi_2(PO_4)_{3-x}F_x$ anode materials for high-performance aqueous lithium ion batteries, *J. Mater. Chem. A*, 2016, **5**, 593–599.
87 J.-Y. Luo, L.-J. Chen, Y.-J. Zhao, P. He and Y.-Y. Xia, The effect of oxygen vacancies on the structure and electrochemistry of $LiTi_2(PO_4)_3$ for lithium-ion batteries: A combined experimental and theoretical study, *J. Power Sources*, 2009, **194**, 1075–1080.

88 C. A. Marianetti, D. Morgan and G. Ceder, First-principles investigation of the cooperative Jahn-Teller effect for octahedrally coordinated transition-metal ions, *Phys. Rev. B: Condens. Matter Mater. Phys.*, 2001, **63**, 224304.

89 A. J. E. Rettie, W. D. Chemelewski, D. Emin and C. B. Mullins, Unravelling Small-Polaron Transport in Metal Oxide Photoelectrodes, *J. Phys. Chem. Lett.*, 2016, **7**, 471–479.

90 A. Moradabadi and P. Kaghazchi, Effect of Strain on Polaron Hopping and Electronic Conductivity in Bulk $LiCoO_2$, *Phys. Rev. Appl.*, 2017, **7**, 064008.

91 S. Loftager, P. Garcia Fernandez, J. A. Aramburu, M. Moreno and J. M. Garcia-Lastra, Stability and Polaronic Motion of Self-Trapped Holes in Silver Halides: Insight through DFT+*U* Calculations, *J. Phys. Chem. C*, 2016, **120**(16), 8509–8524.

92 C. Ku and P. H.-L. Sit, Ab Initio Study of Electron and Hole Polaron Transport in Cobalt(II,III) Oxide Using Oxidation-State Constrained Density Functional Theory, *J. Phys. Chem. C*, 2023, **127**, 13266–13275.

93 A. Rossbach, F. Tietz and S. Grieshammer, Structural and transport properties of lithium-conducting NASICON materials, *J. Power Sources*, 2018, **391**, 1–9.

94 P. Zhang, *et al.*, Water-stable lithium ion conducting solid electrolyte of the $Li_{1.4}Al_{0.4}Ti_{1.6-x}$ $Ge_x(PO_4)_3$ system (x=0∼1.0) with NASICON-type structure, *Solid State Ionics*, 2013, **253**, 175–180.

95 S. Xuefu, *et al.*, High Lithium-Ion-Conducting NASICON-Type $Li_{1+x}Al_xGe_yTi_{2-x-y}(PO_4)_3$ Solid Electrolyte, *Front. Energy Res.*, 2016, **4**, 12.

96 J. M. Garcia-Lastra, J. S. G. Myrdal, R. Christensen, K. S. Thygesen and T. Vegge, DFT+U Study of Polaronic Conduction in Li_2O_2 and Li_2CO_3: Implications for Li–Air Batteries, *J. Phys. Chem. C*, 2013, **117**, 5568–5577.

97 V. L. Deringer, A. L. Tchougréeff and R. Dronskowski, Crystal Orbital Hamilton Population (COHP) Analysis As Projected from Plane-Wave Basis Sets, *J. Phys. Chem. A*, 2011, **115**, 5461–5466.